**Electronic Supplementary Information**

# Iron Tungsten Mixed Composite as a Robust Oxygen Evolution Electrocatalyst

Chizhong Wang, [a] Rong Wang, [ab] Yue Peng, [a] Jianjun Chen [a] and Junhua Li *[a]

[a]*State Key Joint Laboratory of Environmental Simulation and Pollution Control, School of Environment, Tsinghua University, Beijing 100084, PR China.*
[b]*School of Materials Science and Technology, China University of Geosciences, Beijing 100083, PR China.*

**Experimental Section**

*1. Sample preparation.*

$(NH_4)_2Fe(SO_4)_2 \cdot 6H_2O$ (99.95%, Alfa-Aesar) and $Na_2WO_4 \cdot 2H_2O$ (99.5%, Macklin) were purchased and used without further purification. FeW mixed oxides were prepared via a hydrothermal method. $(NH_4)_2Fe(SO_4)_2 \cdot 6H_2O$ and $Na_2WO_4 \cdot 2H_2O$ with different Fe/W molar ratios (95: 5, 3: 1, 1: 1, 1: 3, 1: 0) were dissolved in 7.5mL Milli-Q water (18.2 MΩ cm), respectively. The $Na_2WO_4$ solution was added into the $(NH_4)_2Fe(SO_4)_2$ solution and pH value of the mixture was adjusted to 6 by using NaOH (2 mol $L^{-1}$) or $H_2SO_4$ (1 mol $L^{-1}$) solution. After stirring for 30 min, the mixture was transferred to stainless-steel autoclaves with a Teflon liner (25 mL in volume). The reactors were heated at 180 °C for 5 h and cooled to room temperature. The obtained mixture were centrifuged and rinsed with Milli-Q water for three times and dried at 100 °C for 12 hours.

*2. Electrode preparation.*

Electrode preparation process is shown in Fig. S3. Au substrate was synthesized by radio-frequency magnetron sputtering with an Au layer (100 nm thick) and a metallic Ti interlayer (10 nm thick) deposited on $SiO_2$ or Si substrate (1 × 1 cm). 2.5 mg of the as-prepared sample powder was dispersed into a mixed solution with 970 μL 2-propanol, 20μL $H_2O$ and 10 μL 5 wt.% Nafion solution (Sigma Aldrich). After treated in sonication for 60 min, 40 μL of the ink was drop-casted onto Au substrate and dried at room temperature for 30 min. The sample-loaded Au substrate was connected to conductive wire with an indium solder and sealed with hot glue. The typical exposed geometrical area of the electrode is approximately 0.2 $cm^2$.

*3. Characterizations.*

X-ray diffraction (XRD) patterns were recorded on an X-ray diffractometer (Brucker Advance D8) using a Cu Kα radiation (λ = 0.15405 nm). Raman spectra were measured on a microscopic confocal Raman spectrometer (Renishaw, RM2000) using a laser with wavelength of 633 nm. Transmission electron microscopy (TEM; JEOL, JEM-2100F) with energy-dispersive X-ray spectroscopy (EDS) and scanning electron microscopy (SEM; ZEISS, Geminis 500) were performed to characterize the morphology of electrodes before and post electrochemical tests. X-ray photoelectron spectroscopy (XPS; Thermo Scientific, ESCALAB 250XI) tests were conducted with Al Kα radiation. All binding energies were calibrated using C 1s peak at 284.8 eV as an internal standard.

*4. Electrochemical tests.*

OER performances of FeW electrodes were measured in a three-electrode cell and recorded on an electrochemical potentiostat (CH Instruments, CHI760E). A Hg/HgO electrode (1M KOH, aq.; CH Instruments) was used as a reference and a Pt mesh as a counter electrode. The Hg/HgO reference potential was converted into the reversible hydrogen electrode (RHE) potential according to the Nernst relationship as follows,

$$E(\text{V vs. RHE}) = E(\text{V vs. Hg/HgO}) + 0.059 \times \text{pH} + 0.012, \qquad (1)$$

where 0.012 V is the standard potential for Hg/HgO reference electrode at 25 °C. The potential drop $iR_u$ caused by ionic current flow through the electrolyte between working electrode and counter electrode was corrected using impedance analyzer. 1 M KOH aqueous solution (pH = 13.6) was used as test electrolyte. The electrolyte for FeW and $Fe_2O_3$ electrodes was not further purified as Fe leaching occurred during the test, while $WO_3$ electrode was measured in the $Ni(OH)_x$-

purified KOH electrolyte using the method reported by Boettcher et al. [1] to remove the trace amount of Fe in the KOH electrolyte. Prior to each test, the electrolyte was saturated with $O_2$ for 20 min and continuously purged during experiment.

Electrochemical impedance spectra (EIS) were performed by using a potentiostat (CHI760E) with an impedance analyzer facility. Electrodes were tested at 0.6 V vs. Hg/HgO in 1 M KOH solution with frequency varying from 100 kHz to 0.1 Hz and an AC amplitude of 10 mV. Double-layer capacitances corresponding to the electrochemical surface areas (ECSA) were determined by the scan-rate dependencies of cyclic voltammograms. The capacitive current density was recorded at 0.05 V vs. Hg/HgO in each cyclic voltammogram with the scan rates varying from 5 to 400 mV $s^{-1}$. Catalyst mass change was monitored by quartz crystal microbalance (QCM) electrodes in a resonator circuit apparatus (CHI440). During OER, the variation of loading mass corresponds to the oscillation frequencies, as shown below,

$$\Delta f = \frac{-2f_0^2 \cdot \Delta m}{A \cdot \sqrt{\mu \cdot \rho}}, \quad (2)$$

where $f_0$ (7.995-MHz) is the resonant frequency of the fundamental mode of the crystal, A (0.196 $cm^2$) is the area of the gold disk coated onto QCM electrode, μ ($2.947\times10^{10}$ g $cm^{-1}$ $s^{-2}$) is the shear modulus of quartz, and ρ (2.684 g $cm^{-3}$) is the density of the crystal. The faradaic efficiency of $O_2$ evolution was determined using a rotating ring-disk electrode (RRDE) apparatus (Pine Research). Prior to the RRDE experimental, the FeW disk electrode was measured in chronopotentiometric mode held at 10 mA $cm^{-2}$ for 24 h to stabilize the FeW catalyst. Then RRDE was conducted in $N_2$-saturated 1 M KOH at 1600 rpm, measuring cyclic voltammograms for disk electrode and the Pt ring electrode held at -0.8 V vs. Hg/HgO. The faradaic efficiency was calculated according to the collected disk and ring current with a collection efficiency of 0.2.

*5. Theoretical calculations.*

Density functional theory (DFT) calculations were performed using the Vienna Ab initio Simulation Package (VASP) with the generalized-gradient approximation Perdew-Burke-Ernzerhof (GGA-PBE) exchange-correlation functional. Static electronic correlations were considered for Fe-based structures by applying the Hubbard-U method, where the rotationally invariant implementation of effective U value fixed at 5.3 eV for Fe. Projector augmented-wave (PAW) pseudo potential and a plane-wave cutoff of 500 eV were adopted. The slabs were separated by a vacuum of 15 Å and a Monkhorst−Pack k-point mesh of 5 × 5 × 1 was constructed for converged results. The atom positions were fully relaxed until the residual forces were less than 0.05 eV/Å. Bader charge was calculated as well using the relaxed structure.

The oxygen evolution reaction consists of four elementary steps involving a proton coupled electron transfer (PCET) process:[2]

$$* + H_2O \rightarrow *OH + H^+ + e^-, \quad (2)$$

$$*OH \rightarrow *O + H^+ + e^-, \quad (3)$$

$$*O + H_2O \rightarrow *OOH + H^+ + e^-, \quad (4)$$

$$*OOH \rightarrow * + O_2 + H^+ + e^-, \quad (5)$$

where * represents an adsorption site and *OH, *O and *OOH are the chem-adsorbed reaction intermediates. The highest value among free energy changes $\Delta G_i$ ($i$ = 1, 2, 3, 4) turns all elementary steps downhill. Then the theoretical overpotential is calculated as $\eta = \max\{\Delta G_i\} / e^- - E_{OER}$, where $E_{OER}$ = 1.23 V. The Gibbs free energy of each adsorbed species are calculated,

$$\Delta G_{OH} = E_{*OH}^{Cal} - E_{*}^{Cal} - E_{H_2O(l)} + \frac{1}{2}E_{H_2(g)} + \Delta G_{*OH}^{0}, \quad (6)$$

$$\Delta G_{O} = E_{*O}^{Cal} - E_{*}^{Cal} - E_{H_2O(l)} + E_{H_2(g)} + \Delta G_{*O}^{0}, \quad (7)$$

$$\Delta G_{OOH} = E_{*OOH}^{Cal} - E_{*}^{Cal} - 2E_{H_2O(l)} + \frac{3}{2}E_{H_2(g)} + \Delta G_{*OOH}^{0}, \quad (8)$$

where $\Delta G^0_i$ ($i$ = *OH, *O, *OOH) contains zero potential energy (ZPE), vibrational enthalpy energy ($H_{vib}$) and entropy contribution ($T\Delta S$) for each adsorbate at 300 K. Since the values for $\Delta G^0_i$ change little for different oxide or (oxy)hydroxide materials, we used the values from ref. [3]. In order to avoid calculating the energetic of liquid water, we use the gas-liquid equilibrium that the energy of gaseous $H_2O$ at 0.035 bar and 300 K is equivalent to the standard energy of liquid $H_2O$.

**Results and Discussion**

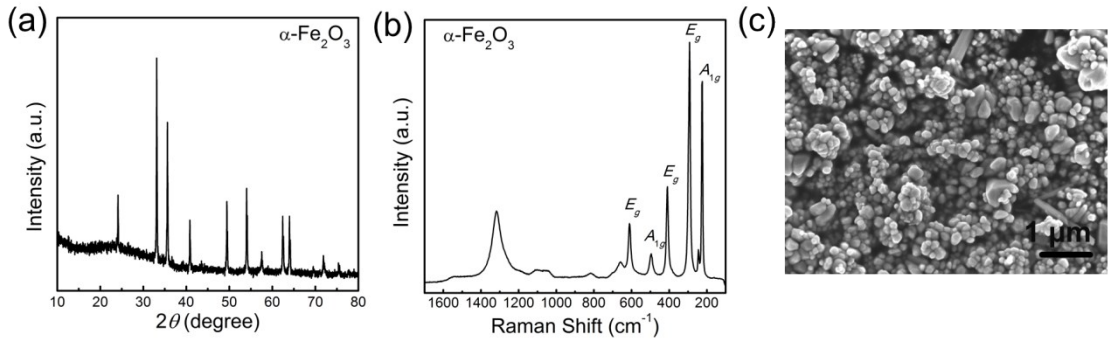


Fig.S1. (a) XRD pattern, (b) Raman spectrum, and (c) top-down view SEM image of α-$Fe_2O_3$.

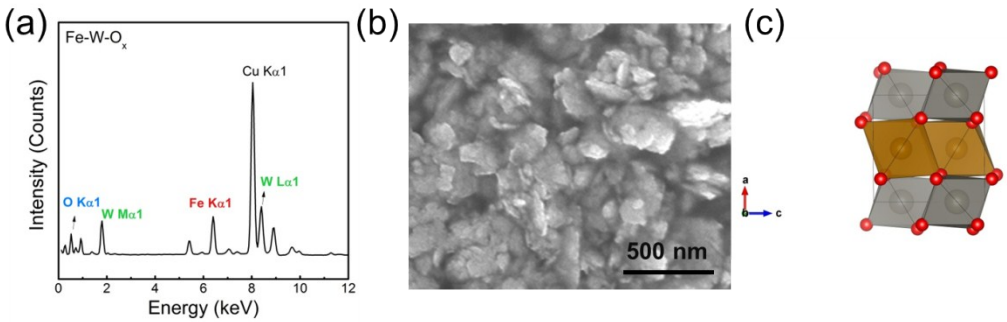


Fig.S2. (a) EDS spectrum derived from STEM image in Fig. 1(c) in the main test, and (b) SEM image of $Fe_3W_1$ sample. (c) Structure of $FeWO_4$ unit cell depicted by VESTA software, where the brown, grey and red balls represent Fe, W and O atoms, respectively.

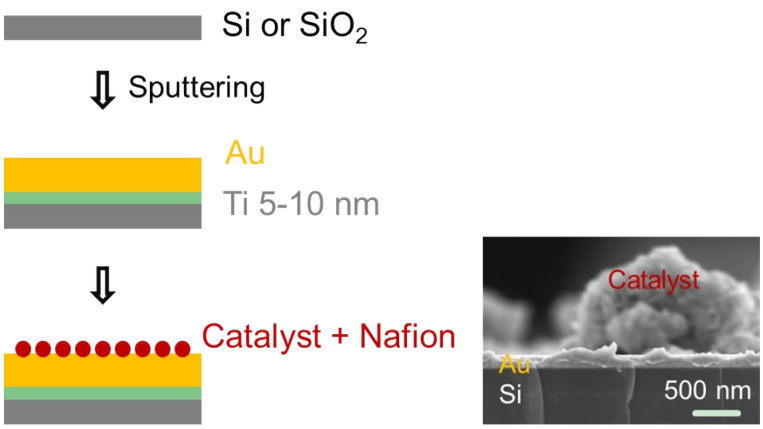


Fig.S3. Schematic depicting the fabrication of a powder-immobilized electrode on an Au film substrate (left) and cross-sectional SEM image (right) of a typical FeW electrode.

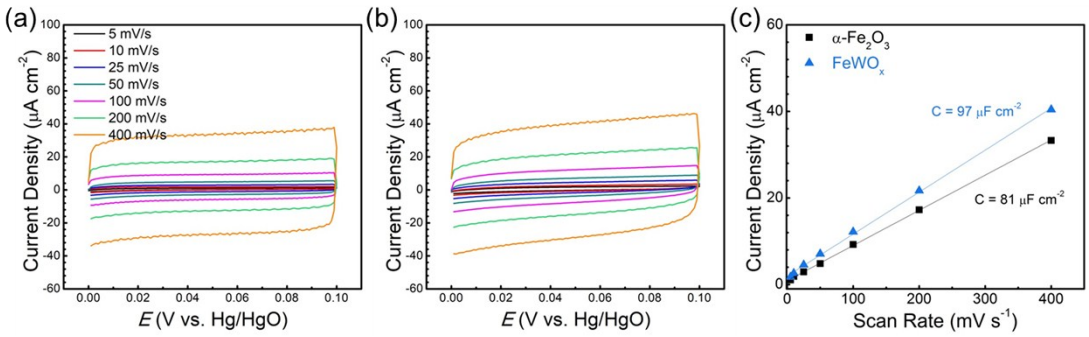


Fig.S4. Cyclic voltammograms for (a) $Fe_2O_3$ and (b) $Fe_3W_1$ electrodes measured with scanning rates varying from 5 to 400 mV $s^{-1}$. (c) The linear relationship between the scan rate and the capacitive current densities at 0.05 V vs. Hg/HgO derived from panels (a) and (b). The capacitances per geometric surface area of $Fe_2O_3$ and FeW were close to each other, indicating the resembled ECSAs for $Fe_2O_3$ and FeW electrodes.

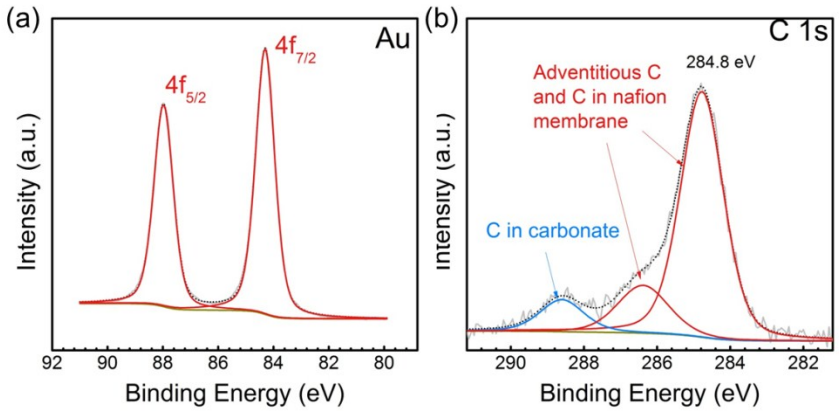


Fig.S5. XPS for (a) Au 4f and (b) C 1s in $Fe_3W_1$/Au electrode after three cyclic voltammograms.

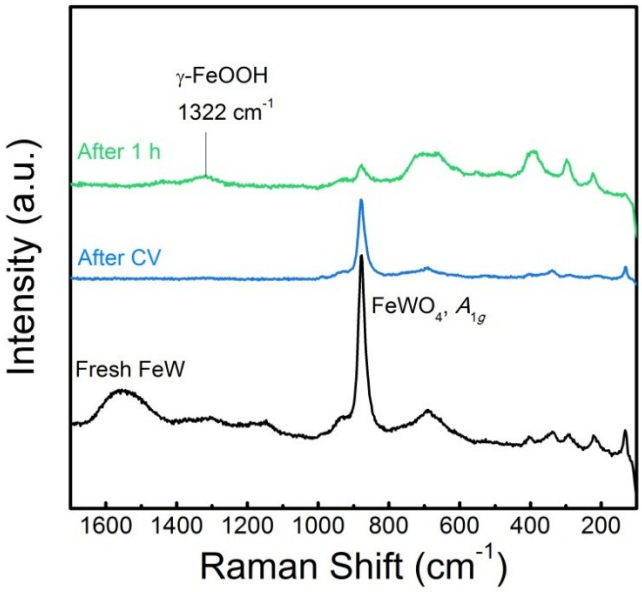


Fig.S6. Raman spectra of the fresh $Fe_3W_1$ electrode deposited on Au substrate, and the electrode after CV and after chronopotentiometry held at 10 mA $cm^{-2}$ for 1 h.

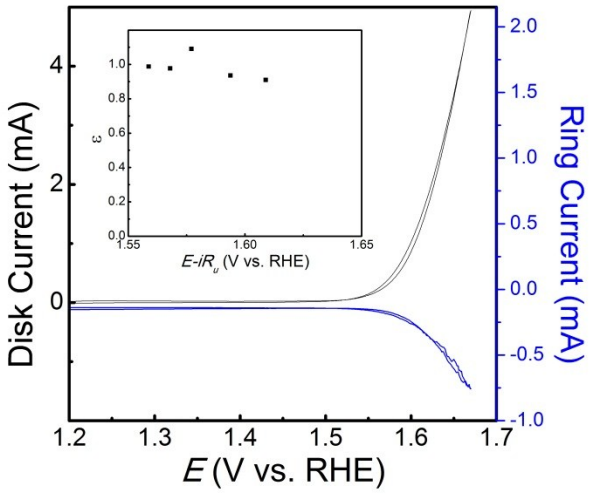


Fig.S7. Cyclic voltammograms for $Fe_3W_1$ disk and Pt ring rotated electrodes. The insert shows that the calculated faradaic efficiencies for oxygen evolution held at different potentials were close to a unit.

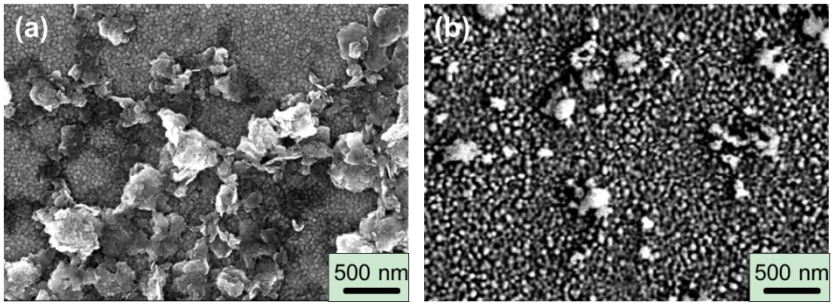


Fig.S8. SEM images for the $Fe_3W_1$ electrode (a) before and (b) post chronopotentiometric test held at 10 mA $cm^{-2}$ for 200 hours.

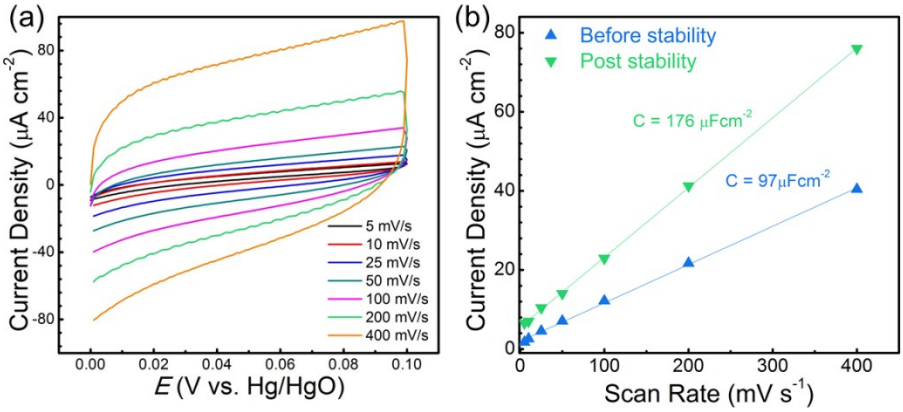


Fig.S9. (a) Cyclic voltammograms for the $Fe_3W_1$ electrode after the 200-hours stability test with scanning rates varying from 5 to 400 mV $s^{-1}$. (b) Linear relationship between the scan rate and the capacitive current densities at 0.05 V vs. Hg/HgO extracted from panel (a) and Fig. S5(b).

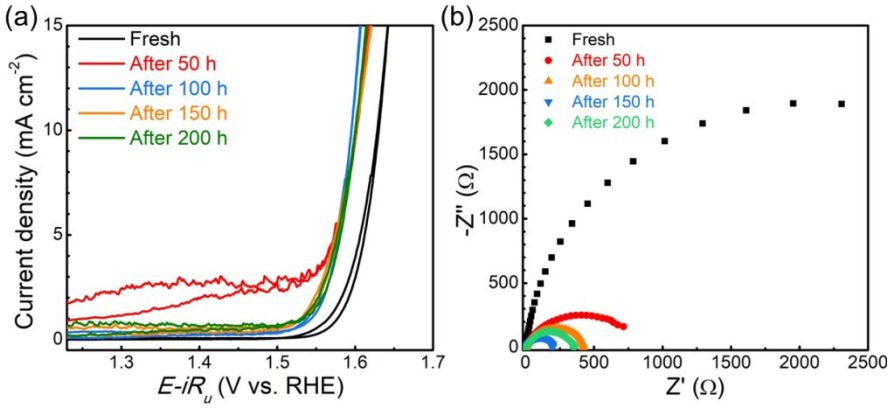


Fig.S10. (a) Cyclic voltammograms and (b) electrochemical impedance Nyquist plots for the $Fe_3W_1$ electrode tested after the chronopotentiometry held at 10 mA $cm^{-2}$ for 0, 50, 100, 150, and 200 hours, respectively.

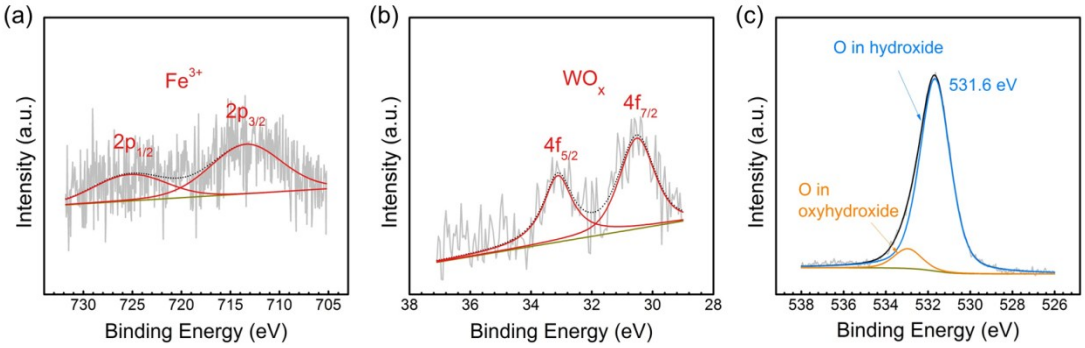


Fig.S11. XPS (a) Fe 2p, (b) W 4f, and (c) O 1s for the $Fe_3W_1$ electrode after chronopotentiometric test held at 10 mA $cm^{-2}$ for 200 hours.

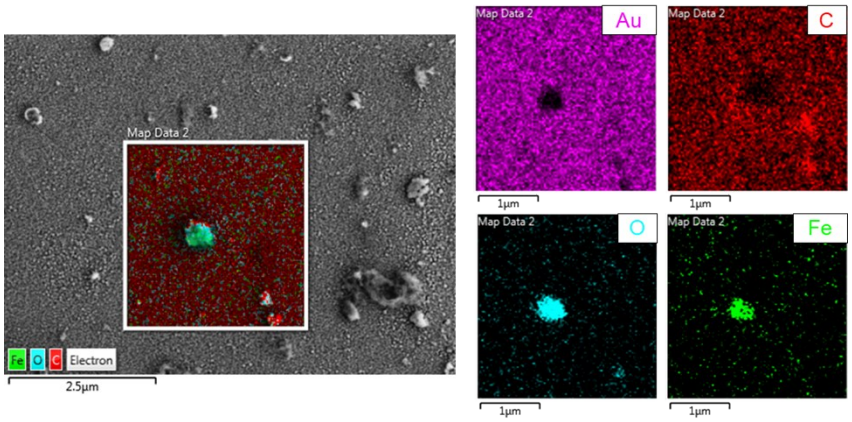


Fig.S12. SEM and EDS element mapping images for the $Fe_3W_1$ electrode after chronopotentiometric test held at 10 mA $cm^{-2}$ for 200 hours.

Based on the XPS and Raman results, a feature of γ-FeOOH phase was observed after CV and chronopotentiometric tests. Hence, we have chosen W-substituted FeOOH to represent the FeW mixed oxide and the (010) facet with the lowest energy for interlayer structure was adopted. Two type of reaction sites for Fe-W structures were considered: (1) [$FeO_6$] and [$WO_6$] octahedrons are

sharing one corner, where Fe–O–Fe acts as the adsorption site for OER intermediates; (2) [$FeO_6$] and [$WO_6$] octahedrons are sharing one edge with two μ-oxo bridge bondings, where Fe–O–W is the reactive site. In addition, structures for pure γ-FeOOH (010) and hexagonal-$WO_3$ (001) were calculated as well to investigate the adsorption energies over Fe and W sites, respectively.

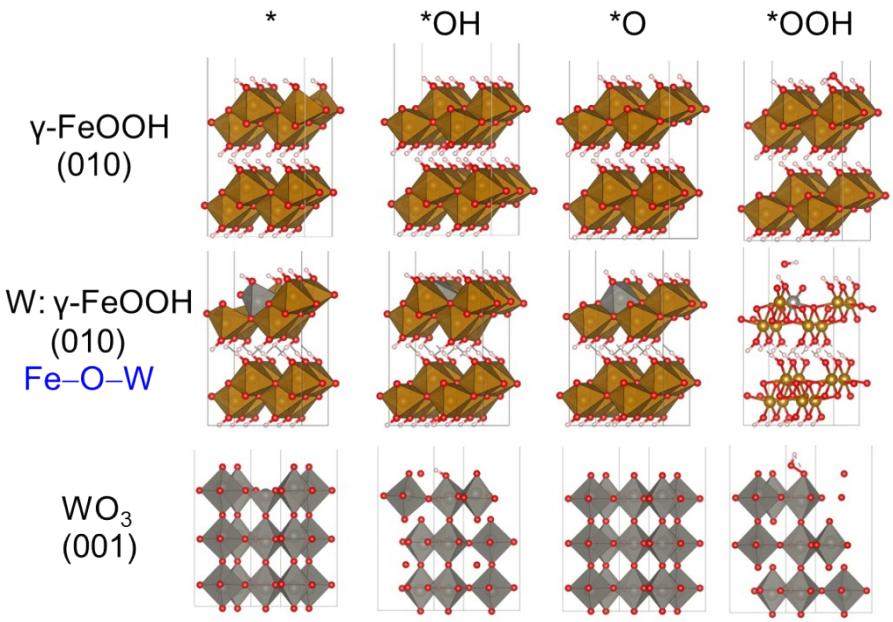


Fig.S13. Calculated structures of the OER intermediates over pure γ-FeOOH (010), W: γ-FeOOH (010) with W and Fe anions sharing a common octahedral edge, and hexagonal $WO_3$ (001). The structure for *OOH adsorbed on W–$O_{vac}$–Fe site could not be relaxed within 400 self-consistent steps until residual maxima force was less than 0.05 eV/Å. The energy barrier was too large to undergo an O–O bonding process and to form a stable *OOH structure on the W–$O_{vac}$–Fe site.

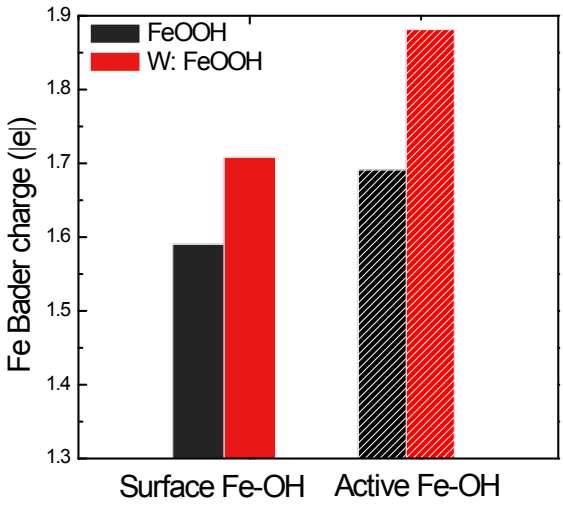


Fig.S14. Fe Bader charges calculated based on the relaxed Fe–OH structures for γ-FeOOH and W: γ-FeOOH. Surface Fe–OH (solid) represents the average value derived from the Bader charges of all surface Fe sites, while active Fe–OH (shadowed) represents the Bader charges calculated from the OER-active Fe sites. It was found that two types of Bader charges increased with the W introduction. Note that a larger value for Bader charge corresponds to a higher chemical valence for the metal site. The results indicated that the presence of W at the surface could induce a charge transfer between Fe and W sites and lead to the formation of high-valent $FeO_x$ species.

Table S1. Fe/W molar ratio for FeW mixed oxides determined by ICP-OES; overpotentials at 10 mA $cm^{-2}$, Tafel slopes and mass-based TOF at overpotential of 400 mV for $Fe_2O_3$, $WO_3$ and FeW electrodes.

| | Fe/W ratio | Overpotential ($\eta$) at 10 mA $cm^{-2}$ / V | Tafel slope / mV $dec^{-1}$ | $TOF_m$ at $\eta$ = 400 mV / $s^{-1}$ |
|---|---|---|---|---|
| α-$Fe_2O_3$ | – | 0.55 | 56.2 | 0.0015 |
| $Fe_{0.95}W_{0.05}$ | 3.11 | 0.43 | 49.6 | 0.022 |
| $Fe_3W_1$ | 1.58 | 0.41 | 51.7 | 0.041 |
| $Fe_1W_1$ | 1.15 | 0.44 | 53.4 | 0.036 |
| $Fe_1W_3$ | 0.87 | 0.44 | 55.5 | 0.038 |
| $WO_3$ | – | – | 90.6 | 0.00048 |

Table S2. Series resistances and charge-transfer resistances fitted from Nyquist plots for electrochemical impedance spectra of α-$Fe_2O_3$, $WO_3$ and $FeWO_x$ electrodes using Randles equivalent circuit.

| | $R_u$ / Ω | $R_{ct}$ / Ω |
|---|---|---|
| α-$Fe_2O_3$ | 4.8 | 26420 |
| $Fe_{0.95}W_{0.05}$ | 5.3 | 2694 |
| $Fe_3W_1$ | 5.8 | 2180 |
| $Fe_1W_1$ | 5.9 | 4158 |
| $Fe_1W_3$ | 6.6 | 2923 |
| $WO_3$ | 8.3 | 44913 |

Table S3. Calculated binding energy for *OH, *O and *OOH intermediates adsorbed on γ-FeOOH, W: γ-FeOOH and *h*-$WO_3$.

| | $\Delta G_{OH}$ /eV | $\Delta G_O$ / eV | $\Delta G_{OOH}$ / eV |
|---|---|---|---|
| γ-FeOOH | –0.311 | 1.836 | 3.040 |
| W: γ-FeOOH | –0.132 | 1.498 | 3.411 |
| *h*-$WO_3$ | 2.279 | 4.363 | 4.707 |

Table S4. Calculated Gibbs free energy differences for each elementary step depicted in Fig. 5(a) in the main text.

| | $\Delta G_1$ / eV | $\Delta G_2$ / eV | $\Delta G_3$ / eV | $\Delta G_4$ / eV | $\eta$ / V |
|---|---|---|---|---|---|
| γ-FeOOH | –0.311 | 2.146 | 1.205 | 1.880 | 0.92 |
| W: γ-FeOOH | –0.132 | 1.630 | 1.914 | 1.509 | 0.68 |
| *h*-$WO_3$ | 2.131 | 2.719 | -0.215 | 0.286 | 1.49 |

**Reference**


[1] L. Trotochaud, S. L. Young, J. K. Ranney, S. W. Boettcher, *J. Am. Chem. Soc.* **2014**, *136*, 6744-6753.

[2] J. Rossmeisl, Z. W. Qu, H. Zhu, G. J. Kroes, J. K. Nørskov, *J. Electroanal. Chem.* **2007**, *607*, 83-89.

[3] B. Zhang, X. Zheng, O. Voznyy, R. Comin, M. Bajdich, M. García-Melchor, L. Han, J. Xu, M. Liu, L. Zheng, F. P. García de Arquer, C. T. Dinh, F. Fan, M. Yuan, E. Yassitepe, N. Chen, T. Regier, P. Liu, Y. Li, P. De Luna, A. Janmohamed, H. L. Xin, H. Yang, A. Vojvodic, E. H. Sargent, *Science* **2016**, *352*, 333-337.